https://doi.org/10.5194/egusphere-2025-4338
Preprint. Discussion started: 14 January 2026

Global transport of upper-tropospheric tropical tracers: multi-year insights from idealized simulations

Lianet Hernández Pardo[1], Joachim Curtius[1], Patrick Jöckel[2], Moritz Menken[2], and Anna Possner[1]

[1]Institute for Institute for Atmospheric and Environmental Sciences, Goethe University Frankfurt, Frankfurt am Main, Germany.
[2]Deutsches Zentrum für Luft- und Raumfahrt, Institut für Physik der Atmosphäre, Oberpfaffenhofen, Germany

Correspondence: Lianet Hernández Pardo (hernandezpardo@iau.uni-frankfurt.de)

Abstract. Recent studies suggest that significant aerosol formation occurs in the tropical upper troposphere (UT). However, the impact of these particles at lower levels remains poorly understood. We present results from multi-year global EMAC simulations investigating the downward transport of UT tracers and their resulting spatial distribution. Nineteen idealized tracers were released in the tropical UT and subjected to resolved-scale advection, parameterized convection, turbulent mixing, and wet/dry deposition. Transport timescales are highly sensitive to source extent: the age of air at 500 hPa is ≈ 45 days for tropical-wide tracers, compared to over 250 days for regional continental sources, reflecting the importance of mixing and dilution. A complementary time-to-threshold diagnostic reveals faster transport pathways, with all source regions exhibiting descent times shorter than 7 days to reach 10% of the source average. Advection dominates vertical transport, with convective and vertical diffusion parameterizations contributing marginally. Injection height exerts a stronger influence on descent time than parameterized transport or particle size in the 20–100 nm range. Tracer maxima are typically advected east of their source centers, resulting in significant concentrations ($\approx$ 10–15$\%$ of source values) in the mid-troposphere. Offline calculations show that, for initial particle numbers below $\approx 6 \times 10^7$ kg^{-1}, the mid-troposphere values predicted by the model are reduced by less than 10% when coagulation is considered, but substantial deviations occur at higher concentrations. These results provide quantitative constraints on particle transport efficiency and inform expectations for aerosol distributions following UT nucleation events.

1 Introduction

A particular pattern in the global distribution of aerosols, characterized by high concentrations of ultrafine particles (mostly nucleation- and Aitken-mode particles) in the tropical upper troposphere (UT), between $\approx$ 9–12 km altitude, has been documented over the last three decades (e.g., Clarke, 1993; Clarke et al., 1999; de Reus et al., 2001; Lee et al., 2003; Minikin et al., 2003; Heintzenberg et al., 2011; Andreae et al., 2018; Williamson et al., 2019). These particles have been attributed to nucleation occurring in the outflow of deep convective clouds, associated with the transport of precursor gases (sulfuric acid and/or organic vapors) from the atmospheric boundary layer (Clarke et al., 1999; de Reus et al., 2001; Froyd et al., 2009; Weigelt et al., 2009; Heintzenberg et al., 2011; Weigel et al., 2011; Andreae et al., 2018; Curtius et al., 2024).

https://doi.org/10.5194/egusphere-2025-4338
Preprint. Discussion started: 14 January 2026

Enhanced aerosol content in the UT has important implications for Earth's radiation budget and may serve as a source of cloud condensation nuclei (CCN) following particle growth and downward transport (Wang et al., 2016; Varanda Rizzo et al., 2018; Andreae et al., 2018; Williamson et al., 2019; Curtius et al., 2024). For this reason, accurately representing these aerosols is necessary in weather and climate simulations. Attempts to simulate particle production in the UT have been reported by, for instance, Zhang et al. (2010); Yu et al. (2010); English et al. (2011); Ekman et al. (2012); Watson-Parris et al. (2019). However, it remains challenging to emulate the UT aerosol enhancement within the tropics because of the difficulties in adequately representing sources and sinks of precursor gases, chemical reactions leading to new particle formation, and transport mechanisms. Such representation depends largely on physical parameterizations, including surface emissions, cloud microphysics, convection, and aerosol/gas chemistry, as well as on dynamical feedbacks.

Specifically, transport from the tropical UT may follow different pathways. While transient phenomena –such as low- and high-pressure systems at the synoptic scale, and even mesoscale convective systems– can induce significant short-term variability in the atmospheric circulation, the general circulation patterns dominate in the long term. From a general circulation perspective, part of the UT air may be transported poleward within the Hadley cell and descend in the subtropics, or ascend further into the lower stratosphere above equatorial regions, where it may then be transported poleward and descend at high latitudes within the stratospheric (Brewer-Dobson) circulation on timescales of over two years (Brewer, 1949; Dobson and Massey, 1956; Brock et al., 1995). These mechanisms are consistent with multi-year statistics of aerosol observations showing a pronounced latitudinal gradient of aerosol concentration in the mid-to-upper troposphere, decreasing poleward from the tropics (e.g., Clarke and Kapustin, 2002). Nonetheless, significant longitudinal variability can also arise, even in long-term statistics, due to the distribution of semi-stationary high-pressure systems in the tropics (e.g., the Walker circulation). Moreover, although freshly nucleated particles (on the order of 1–10 nm) have negligible sedimentation rates (Seinfeld and Pandis, 2016), sedimentation can eventually become important once they grow via condensation and coagulation – particularly in the stratosphere, where particle lifetimes are $\mathcal{O}(1)$ year and sizes can grow significantly larger than in the upper troposphere (Hamill et al., 1997).

Downward transport has been proposed by several observational studies as a source of aerosols for the atmospheric boundary layer (e.g., Raes, 1995; Covert et al., 1996; Clarke et al., 1998, 1999; Raes et al., 2000; Wang et al., 2016; Franco et al., 2021; Machado et al., 2021). The modeling study of Mann et al. (2012) suggests particle transport and growth from the tropical UT to the subtropical free troposphere. For a limited area over the unperturbed Amazon rain forest, the simulations of Zhao et al. (2020) found net downward transport over a wide altitude range, from the UT to the lower troposphere. However, the underlying mechanisms behind this downward transport are not yet thoroughly understood. For example, the relative roles of isolated and organized convection versus synoptic- or large-scale subsidence remain unexplored.

Observations typically provide only discrete (in space and/or time) snapshots of the atmospheric state, making it difficult to disentangle the transport history of the sampled air masses. Nonetheless, studies suggest that other atmospheric layers, beyond the UT, may also act as aerosol sources, potentially masking UT contributions. For example, Lampilahti et al. (2021), and references therein, suggested that particles may be nucleated at the interface between the residual layer and the free troposphere after sunrise, via photochemical reactions of gases released at the surface, and then entrained into the mixed layer later in the

https://doi.org/10.5194/egusphere-2025-4338
Preprint. Discussion started: 14 January 2026

day. This is supported by studies finding a correlation between elevated ultrafine particle counts at the surface and the onset of convection in the morning mixing layer (e.g., Nilsson et al., 2001). Consequently, the extent to which UT-nucleated particles can be efficiently transported downward to reach the atmospheric boundary layer remains highly uncertain. In other words, it is unclear over what altitude range CCN budgets are dominated by UT-nucleated particles that grow during descent, and from which levels boundary-layer or free-troposphere sources dominate.

Based on time-averaged particle and CCN budgets at low levels in one-year global simulations, Merikanto et al. (2009) showed that sulfate particles nucleated in the free troposphere and UT were nearly zonally distributed at ground level, with maximum concentrations near the tropics likely associated with the downward branch of the Hadley cell. These particles appeared to play a key role in marine regions with weak primary emissions (mainly regions of low wind speed). However, while most particles in their simulations are generated in the UT, they do not distinguish between free-tropospheric and UT particles reaching the lower troposphere.

In a recent study, Wang et al. (2023) used a 4-km resolution regional nest within a global model to show that, across a ≈ 1000 km domain in the Amazon and over a timescale of a few days, aerosols formed in the UT seldom reached the boundary layer. Instead, most boundary-layer CCN arriving from higher levels originated outside the region. Because their analysis was limited to a brief period and relatively small domain, the question remains whether (and how) UT aerosols might be transported downward on longer timescales or across broader spatial scales. Here, we address this gap by combining multi-year global simulations with idealized tracers initialized in the UT. To achieve such extended temporal and spatial coverage, we necessarily use a coarser resolution than Wang et al. (2023), yet we hypothesize that this approach allows us to isolate large-scale transport pathways and capture the long-term circulation patterns capable of carrying UT air –and the aerosols it contains– downward into the lower troposphere.

To separate transport effects from uncertainties in aerosol formation and growth, we employ inert, passive tracers under an idealized initialization scheme, assuming a constant size distribution. Analyzing typical transport timescales and pathways provides a first step toward characterizing the fate of freshly-nucleated UT particles. In particular, we focus on how large-scale (synoptic- and global-scale) downward transport mechanisms determine the pathways that UT particles may follow. To estimate particle survival rates, besides accounting for intrinsic dilution caused by numerical and parameterized mixing, we incorporate removal processes via wet scavenging, sedimentation, and dry deposition. The uncertainties associated with neglecting particle growth are assessed through a sensitivity test using a larger mean size and offline estimates of the impact of coagulation.

The design of the numerical experiments and the analysis methods is detailed in Section 2. Results, including tracer transport timescales and spatial patterns of tracer number mixing ratio, are presented in Section 3. A discussion of the relevance and applicability of these results is provided in Section 4, followed by concluding remarks in Section 5.

2 Methods

We employed the EMAC model (Jöckel et al., 2006, 2010), which is a combination of the ECHAM5 atmospheric general circulation model (Roeckner et al., 2003) with the Modular Earth Submodel System (MESSy, Jöckel et al, 2005, 2010) (MESSy

https://doi.org/10.5194/egusphere-2025-4338
Preprint. Discussion started: 14 January 2026

Jöckel et al., 2005, 2010). A T106 triangular spectral truncation was chosen for the spherical harmonics dynamical core, with a corresponding 1.125° resolution (∼125 km at the Equator) quadratic Gaussian grid for the evaluation of advection terms and subgrid scale parameterizations. Tracer advection follows the flux-form semi-Lagrangian scheme of Lin and Rood (1996) on the quadratic Gaussian grid. In the vertical dimension, equations are solved using finite differences (Burridge and Haseler, 1977; Simmons and Burridge, 1981), based on a hybrid pressure-based terrain-following coordinate with 90 levels and top at 1 Pa.

A semi-implicit scheme is used for time integration, with implicitness factors $\beta_{DT} = 0.8$ for divergence, temperature and surface pressure and $\beta_{ZQ} = 1$ for vorticity, and with reference temperature and surface pressure of 300 K and 800 hPa, respectively (Robert et al., 1972; Robert, 1981, 1982). A time filter is used to limit the growth of spurious computational modes similar to Asselin (1972), with a time filtering coefficient $\epsilon = 0.1$.

Two simulations were performed, with durations of 11 and 2.5 years, respectively, starting on January 1, 1998. An integration time step length of 240 s was employed for the 2.5-year simulation and the first 2 years and two months of the 11-year simulation. At later times in the 11-year simulations, the integration time step length was reduced to 60 s to prevent computational instabilities. In our analyses, we consider a spin-up period of 1 year.

Radiation processes and surface temperature parameterization follow the original ECHAM5 approaches, the former modified according to Dietmüller et al. (2016). The scheme of Emmerichs et al. (2021) is employed to represent land-atmosphere exchange and vertical diffusion. Orographic gravity waves and low level drag are represented by the scheme of Lott and Miller (1997); Lott (1999), as in ECHAM5. Cloud microphysics are parameterized following Lohmann and Roeckner (1996), with cloud cover calculations following Sundqvist (1978); Sundqvist et al. (1989). A mass flux convection scheme is applied (Tiedtke, 1989), with the closure assumptions of Nordeng (1994).

Initial conditions were derived from ERA5, the fifth generation ECMWF (European Center for Medium-Range Weather Forecasts) reanalysis (Hersbach et al., 2020). Surface boundary conditions (sea surface temperature and sea ice concentration) are based on a climatology computed as the multi-year monthly mean over 2000–2019, using output from the Max Planck Institute for Meteorology Earth System Model version 1.2 (MPI-ESM1.2) model prepared for the Coupled Model Intercomparison Project (CMIP6) (Schupfner et al., 2023; Müller et al., 2018; Mauritsen et al., 2019).

To analyze transport pathways and associated timescales from the tropical UT, we introduced 19 idealized tracers (Table 1) via MESSy's submodel PTRAC (Jöckel et al., 2008). The tracers were initialized and forced in the tropical UT between 200–300 hPa, except in some cases (suffix "_higher" in the tracer name), in which the forcing region was shifted to 150–250 hPa to evaluate the impact of uncertainties in the height of the tracer layer. Tracer initialization and forcing used the MESSy submodels IMPORT_GRID and TNUDGE (Kerkweg et al., 2006b; Kerkweg and Jöckel, 2015). Different longitude intervals were defined for the forcing region: all over the Tropics (prefix "tropical_" in the tracer names), restricted to South American longitudes and centered in the Amazon (prefix "amazon_"), over the Sub-Saharan Africa (prefix "africa_"), and over the Maritime Continent (prefix "mar-cont_"). By considering these different forcing regions, we aim to understand the potential implications of longitudinal gradients in the aerosol source region for the transport pathways and timescales. The focus on

https://doi.org/10.5194/egusphere-2025-4338
Preprint. Discussion started: 14 January 2026

continental regions is due to their higher potential for UT secondary aerosol nucleation compared to maritime regions, given the strong coupling between vegetation emissions and convective uplift.

A set of 5 tracers followed an "age of air" approach ("aoa" string in the tracer names in Table 1), in which the tracer number mixing ratio N_{aoa} varied quasi-linearly (i.e., step wise) with time within the forcing region and were subject to transport outside of it (Eq. 1). The transport operator $\mathcal{T}$ includes resolved advection, as well as parameterized turbulent diffusion and convection.

$$N_{\text{aoa}}(t,P,\phi,\lambda) = \begin{cases} N_* \max\left\{0,\ t-1+e^{-2\left(\frac{\phi}{\phi_0}\right)^2}\right\}, & \text{if } \phi\in[-\phi_0,\phi_0],\ \lambda\in[\lambda_{\min},\lambda_{\max}],\ P\in[P_{\min},P_{\max}]. \\ \mathcal{T}\left(N_{\text{aoa}}\right), & \text{otherwise,} \end{cases} \tag{1}$$

where t is the time in days; ϕ and λ are the latitude and longitude, respectively, in degrees; P is the pressure, in hPa; $N_* = 2.08\times10^{16}$ kg^{-1} and $\phi_0 = 20°$.

The age of air is defined as the time elapsed since a parcel of air was last in contact with a specific source region. Due to mixing, the age at a given location is better described statistically by the "age spectrum", denoted by $\Gamma(\tau)$, which represents the fraction of air mass with transit time τ. The *mean age of air* corresponds to the first moment of this distribution:

$$\langle\tau\rangle = \int_0^\infty \tau\,\Gamma(\tau)\,d\tau, \tag{2}$$

representing the average transit time from the source to the target location (Hall and Plumb, 1994; Waugh and Hall, 2002).

In practice, $\langle\tau\rangle$ can be estimated using a tracer that is uniformly distributed within the source region and increases linearly in time, with no sources or sinks elsewhere. Outside the source, the tracer is passively transported. At a given location, $\langle\tau\rangle$ is estimated by subtracting the local tracer value from the value in the source region and dividing by the known rate of increase in the source region (i.e., the linear slope). This approach is described by Podglajen and Ploeger (2019) and references therein. Note that, for tracers defined according to Eq. 1, N_{aoa} is not uniform within the forcing region –it is maximum at the Equator and decreases toward the maximum value on the previous day plus e^{-2} at $\phi = \pm20°$. Smoothing the tracer spatial distribution in this way alleviates issues associated with advection near sharp gradients. However, even in the presence of spatial inhomogeneities, this approach remains valid for deriving $\langle\tau\rangle$ with resolution of 1 day, given that the tracer values across the forcing region do not overlap in time.

To analyze the impact of size-dependent aerosol sinks on the transport patterns, the number mixing ratios of 6 tracers were kept constant within the forcing region throughout the simulation ("constant" string in the tracer names in Table 1), mimicking a continuously-replenished aerosol reservoir:

https://doi.org/10.5194/egusphere-2025-4338
Preprint. Discussion started: 14 January 2026

Table 1. Summary of the idealized tropical upper-tropospheric tracers and their specifications

tracer name	region	forcing	$\lambda_{\min};\lambda_{\max}$ (° E)	$P_{\min}; P_{\max}$ (hPa)	sinks	r_m (nm)	conv	diff
tropical_aoa	Tropics	age of air	−180;180	200; 300	-	-	yes	yes
amazon_aoa	Amazon	age of air	−79;−39	200; 300	-	-	yes	yes
africa_aoa	Sub-Saharan Africa	age of air	5;45	200; 300	-	-	yes	yes
mar-cont_aoa	Maritime Continent	age of air	100;140	200; 300	-	-	yes	yes
tropical_aoa_higher	Tropics	age of air	−180;180	150; 250	-	-	yes	yes
tropical_constant_no_ssdd	Tropics	constant	−180;180	200; 300	no	-	yes	yes
tropical_constant_with_ssdd	Tropics	constant	−180;180	200; 300	yes	20	yes	yes
amazon_constant_with_ssdd	Amazon	constant	−79;−39	200; 300	yes	20	yes	yes
africa_constant_with_ssdd	Sub-Saharan Africa	constant	5;45	200; 300	yes	20	yes	yes
mar-cont_constant_with_ssdd	Maritime Continent	constant	100;140	200; 300	yes	20	yes	yes
tropical_constant_bigger_with_ssdd	Tropics	constant	−180;180	200; 300	yes	100	yes	yes
tropical_stgrd	Tropics	constant	−180;180	200; 300	yes	20	yes	yes
amazon_stgrd	Amazon	constant	−79;−39	200; 300	yes	20	yes	yes
africa_stgrd	Sub-Saharan Africa	constant	5;45	200; 300	yes	20	yes	yes
mar-cont_stgrd	Maritime Continent	constant	100;140	200; 300	yes	20	yes	yes
amazon_stgrd_bigger	Amazon	constant	−79;−39	200; 300	yes	100	yes	yes
amazon_stgrd_higher	Amazon	constant	−79;−39	150; 250	yes	20	yes	yes
amazon_stgrd_noconv	Amazon	constant	−79;−39	200; 300	yes	20	no	yes
amazon_stgrd_nodiff	Amazon	constant	−79;−39	200; 300	yes	20	yes	no

$$N_{\text{cnt}}(t,P,\phi,\lambda) = \begin{cases} N_* \, e^{-2\left(\frac{\phi}{\phi_0}\right)^2}, & \text{if } \phi \in [-\phi_0, \phi_0], \\ & \lambda \in [\lambda_{\min}, \lambda_{\max}], \\ & P \in [P_{\min}, P_{\max}], \\ & t > t_0. \\ \mathcal{T}\big(N_{\text{cnt}}\big) + \mathcal{F}\big(N_{\text{cnt}}\big), & \text{otherwise,} \end{cases} \tag{3}$$

where $t_0 = 0$, and $\mathcal{F}$ represents the sources/sinks associated with sedimentation, wet scavenging and dry deposition. According to Eq. 3, the average of N_{cnt} within the forcing region (N_{ref}) is $\approx 1.25 \times 10^{16}$ kg^{-1}.

Some of the constant tracers were subject to sedimentation, wet scavenging, and dry deposition (i.e., $\mathcal{F}\big(N_{\text{cnt}}\big) \neq 0$, suffix
155 "with_ssdd"), where "ssdd" denotes the inclusion of these subgrid-scale processes as parameterized by Tost et al. (2006) and Kerkweg et al. (2006a), via the MESSy submodels SEDI, SCAV, and DDEP, respectively. In contrast, other tracers were only transported (i.e., $\mathcal{F}\big(N_{\text{cnt}}\big) = 0$, suffix "no_ssdd").

In order to apply these parameterizations, the tracers were assumed to represent aerosol particles distributed according to a log-normal function, with mean radius $r_m = 20$ nm and geometric standard deviation equal to 1.6. The value of r_m was

https://doi.org/10.5194/egusphere-2025-4338
Preprint. Discussion started: 14 January 2026

increased to 100 nm for one of the constant tracers ("bigger" string in the tracer names), to estimate the impact of uncertainties in the particle size on the parameterized sinks.

Adjusting the diagnostic framework to consider not only $\langle\tau\rangle$ – which reflects the mass-weighted average over the full tracer age distribution $\Gamma(\tau)$ – but also transit times in the left tail of the distribution, enables the characterization of faster, more immediate impacts on the target region. Specifically, the elapsed time between tracer release and the moment a given fraction of the forcing-region mean number mixing ratio N_{ref} is reached at a location can serve as a proxy for the influence of small amounts of material transported over relatively short timescales. We define this metric as the *time-to-threshold* t_p, where p represents the chosen fractional threshold of N_{ref}. Mathematically, this timescale corresponds to the p-th percentile (or quantile) of the tracer age spectrum $\Gamma(\tau)$ at a given location, and is defined by

$$\int_0^{t_p} \Gamma(\tau)\, d\tau = p. \tag{4}$$

This formulation provides a measure of how rapidly a given fraction of tracer mass has arrived from the source, and captures the timing of fast transport components. Together, $\langle\tau\rangle$ and t_p provide complementary perspectives on downward transport.

To diagnose t_p, we introduced eight sets of 12 "staggered" tracers N_{stgrd}, defined identically to N_{cnt} in Eq. 3, except that t_0 is the first day of each month over a full calendar year. These sets of tracers are denoted by the "_stgrd" suffix in the tracer names in Table 1: one set for each forcing region, and four additional sets corresponding to sensitivity tests for the Amazon source region. These include "_bigger" and "_higher" (as described above), and "_noconv"/"_nodiff" tracers for which parameterized convection or turbulent diffusion, respectively, were disabled. These tracers were initialized from January to December 1999 in the 2.5-year simulations starting on January 1, 1998.

It is important to note that the staggered tracers used in this analysis include not only transport but also atmospheric sinks such as wet scavenging, dry deposition, and sedimentation. Consequently, the time-to-threshold metric reflects not the pure transport-derived age spectrum, but a modified or effective age spectrum that is shaped by both transport and removal processes. Mathematically, the distribution being sampled by the diagnostic can be viewed as a filtered age spectrum $\Gamma^*(\tau) = \Gamma(\tau)S(\tau)$, where $S(\tau)$ represents a survival function accounting for tracer loss as a function of age. As such, the resulting timescales represent a convolved measure of both transit and retention, rather than transport alone.

3 Results

To investigate downward transport from the UT, we take the 500 hPa level as a representative reference for the mid-troposphere. Figure1 provides an overview of the simulations, showing time series of the tracer mixing ratio N_{cnt} and age of air $\langle\tau\rangle$ over the full 11-year period. The values are averaged over horizontal areas centered on the forcing regions but extending 10° beyond them in each direction (larger red rectangles in Figure 2), at 500 hPa. The time series evidence a fast increase in $\langle\tau\rangle$ (Figure 1a,b) at the beginning of the simulation, as the target regions progressively fill with air originating from the forcing region. Note that grid points not yet reached by air from the forcing region are treated as missing values and are therefore excluded from the averages.

https://doi.org/10.5194/egusphere-2025-4338
Preprint. Discussion started: 14 January 2026

For the tropical tracers (Fig. 1a), the time series stabilize relatively quickly, reaching a plateau shortly after one year. In contrast, the regional tracers (Fig. 1b) require considerably more time to reach equilibrium (≈ 4 years). This difference reflects the stronger influence of mixing and dilution on the regional tracers compared to the tropical tracers, due to the smaller size of the source region. Typical values of $\langle\tau\rangle$ derived from the tropical tracer are approximately 40–45 days, increasing to approximately 55–65 days when considering the higher source region. Due to stronger dilution, $\langle\tau\rangle$ derived from the regional tracers is about five times older (≈ 260 days) than that derived from the tropical tracers (Fig. 1a,b).

Consistent with the age of air, the 500 hPa area-averaged values of N_{cnt} from the tropics-wide source take approximately one year to reach a plateau (Fig.1c). For this tracer, $N_{\text{cnt}}/N_{\text{ref}}$ plateaus at approximately 0.73, indicating a 27% reduction due to dilution during downward transport. In contrast, when dry deposition, wet scavenging and sedimentation are applied, $N_{\text{cnt}}/N_{\text{ref}}$ stabilizes much faster, albeit at a lower value (≈ 0.15–0.25 for the tropical tracer and ≈ 0.05–0.15 for the regional ones), owing to the sink effect of these processes. Further analysis (not shown) indicated that wet scavenging is by the far the dominant sink in play. Little sensitivity to the role of wet scavenging in relation to variations in r_m over the 20–100 nm range is evident by comparing the default and bigger tropical tracer with sinks in Fig. 1c. A bias in $N_{\text{cnt}}/N_{\text{ref}}$ of around ≈ 0.05 for the tropical tracer with sinks, and ≈ 0.025 for the regional tracers with sinks, before and after the year 2002 is evident in Fig. 1c,d. Given that this discontinuity is only evident in the time series of tracers with sinks, and that the effects of dry deposition and sedimentation are negligible (as noted above), the bias is likely associated with the wet scavenging parameterization and its sensitivity to the integration time step, which was reduced after 2002.

3.1 Tracer transport timescales

In order to delve further into the details of the transport times scales and pathways from the forcing region down to the mid-troposphere, we analyze here the spatial patterns of the age of the air (Fig. 2) and estimate the time elapsed until a given fraction of the forcing region maximum is reached –the time-to-threshold, t_p– for each grid point at 500 hPa, based on the staggered-release tracer sets (Fig. 3).

The mean age of the tropical-sourced air, averaged over time at 500 hPa (Fig. 2a), reveals a pronounced latitudinal distribution. As expected, younger air is predominantly found near the Equator, with $\langle\tau\rangle$ increasing progressively toward the poles. Significant longitudinal variability is also observed, characterized by more rapid downward transport over the Equatorial Pacific Ocean (approximately 8–16 days), followed by the Indian Ocean, regions of Eastern Sub-Saharan Africa, the Northern South Atlantic Ocean, and the northeastern coast of South America (approximately 16–32 days). This distribution aligns with the locations of large-scale subsidence branches of the Walker Circulation and is expected to vary with phase of the El Niño-Southern Oscillation (ENSO), though such variability is not depicted here.

The introduction of non-zero longitudinal gradients via the regional sources allows to distinguish zonal variations in downward transport. Figure 2b indicates that downward transport predominantly occurs below and to the east of the forcing region, likely influenced by upper-tropospheric westerlies when the Intertropical Convergence Zone (ITCZ) shifts north or south and the subtropical jet approaches the source region. Nonetheless, the spatial distribution of $\langle\tau\rangle$ from the regional tracers (Fig. 2b) is consistent with the overall Equatorial-centered pattern evidenced by the Tropical tracer. As mentioned earlier in section 3,

https://doi.org/10.5194/egusphere-2025-4338
Preprint. Discussion started: 14 January 2026

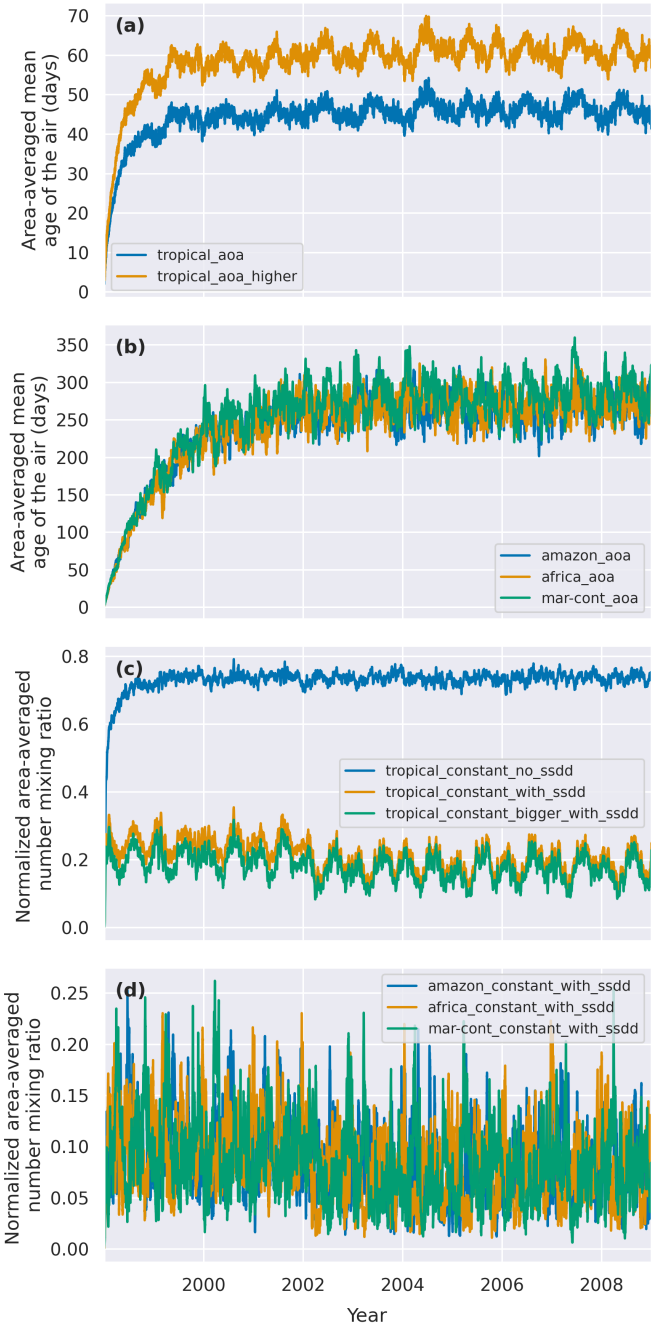

Figure 1. Time series of (a-b) the mean age of the air $\langle \tau \rangle$ and (c-d) the normalized number mixing ratio $N_{\text{cnt}}/N_{\text{ref}}$, averaged at 500 hPa over the outer red polygons in Fig. 2, 3, and 5.

https://doi.org/10.5194/egusphere-2025-4338
Preprint. Discussion started: 14 January 2026

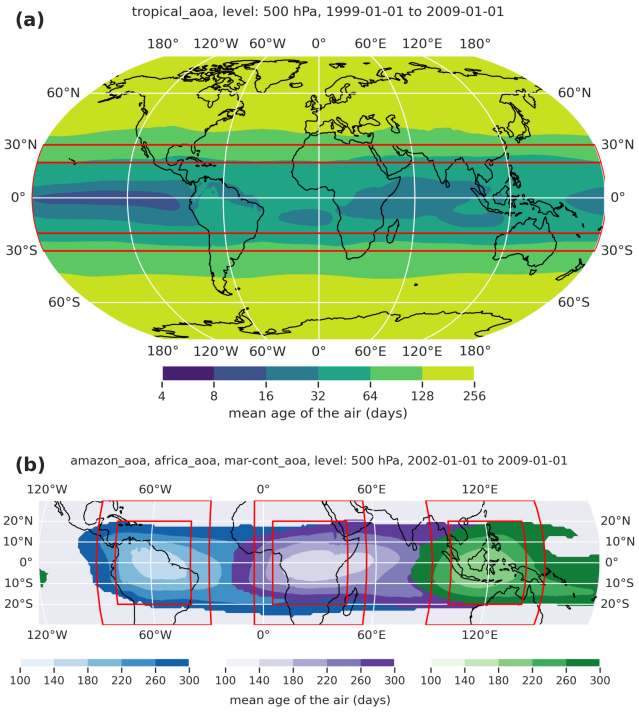

Figure 2. Mean age of air $\langle\tau\rangle$ at 500 hPa, averaged over the simulation period after January 1, 1999 for the tropical tracer (tropical_aoa) and after January 1, 2002 for the regional tracers (amazon_aoa, africa_aoa, and mar-cont_aoa). Red inner rectangles indicate the forcing regions, while red outer rectangles show the averaging regions referenced in other figures (see text for details).

$\langle\tau\rangle$ derived from the regional sources are much longer than that derived from the tropical tracer, with values above 180 days in most of the grid points directly below the regional sources.

Extending the analysis beyond the mean age of air to include lower percentiles of $\Gamma(\tau)$, via the time-to-threshold t_p, allows for the characterization of faster, more immediate impacts on the target region. Because the staggered tracers used here to derive t_p include sinks such as wet scavenging, dry deposition, and sedimentation, the resulting timescales also reflect more physically realistic arrival times compared to $\langle\tau\rangle$.

Figure 3 shows the average $t_{10\%}$ from the 12 staggered tracers (i.e., initialized monthly over one year) in each set – Tropics, Amazon, Africa, and Maritime Continent. Note that a 10% threshold is physically relevant, as it is comparable to the fraction of secondary organic aerosols nucleated in the boundary layer relative to the UT in previous numerical studies (e.g., Zhu et al., 2019). Overall, the spatial patterns in Fig. 3 are broadly consistent with the distribution of $\langle\tau\rangle$, but the timescales are considerably shorter, as expected. Values below one week appear across Equatorial regions for all source areas considered.

The dependence of the t_p on the chosen threshold p is illustrated in Fig. 4. It shows that t_p varies approximately as a power law with respect to p. Notably, this power-law relationship is remarkably consistent across the different forcing regions, with timescales from the Tropical source region differing from those of the regional sources by an approximately constant factor of

https://doi.org/10.5194/egusphere-2025-4338
Preprint. Discussion started: 14 January 2026

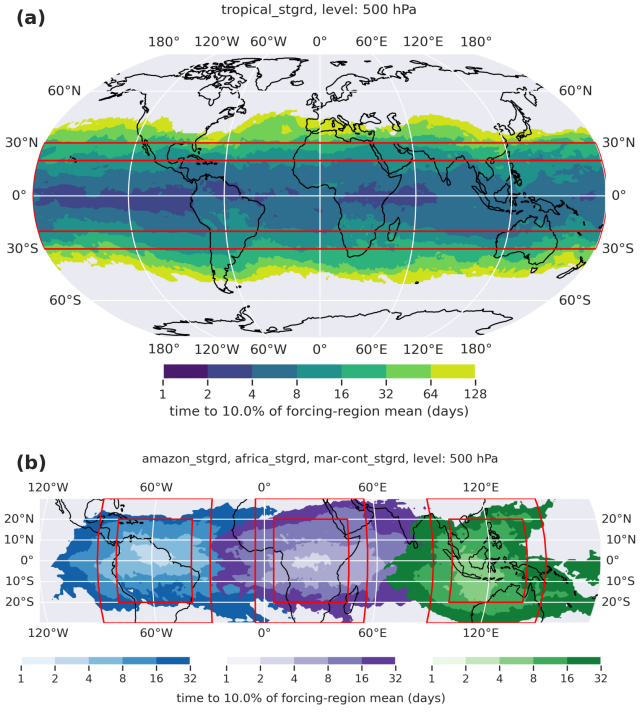

Figure 3. Average time to reach 10% of the mean mixing ratio in the forcing region ($t_{10\%}$) for the Tropical, Amazon, Africa, and Maritime Continent tracers, at 500 hPa. For each source region, $t_{10\%}$ is diagnosed individually from a set of twelve "staggered" tracers, initialized on the first day of each month in 1999 ("_stgrd" suffix in Table 1). The values shown represent the arithmetic mean of these twelve estimates. Red rectangles indicate the forcing and averaging regions as in Fig. 2, for reference.

≈ 2, and little differences across the regional sources (Fig. 4a). Figure 4b shows that the impact of parameterized transport components (convection and turbulent diffusion) is very small overall. Neglecting convection leads to a $\approx 10\%$ increase in the average t_p, while excluding turbulent diffusion is associated with an overall delay of only a $\approx 1\%$ with respect to the default case. The sensitivity of t_p to convection and turbulent diffusion is generally smaller than the sensitivity to the tracer initialization assumptions regarding size and height.

Particularly, the sensitivity of the area-averaged t_p to the height of the forcing region highlights the non-linearity of vertical motions. Raising the source layer by 50 hPa (from 300–200 hPa to 250–150 hPa; $\approx$ 1–1.5 km higher) increases $t_{10\%}$ by ≈ 19 days relative to the baseline (default) tracer, implying a mean descent of ≈ 0.05–0.08 km day^{-1}. By contrast, the baseline tracer has $t_{10\%} \approx 25$ days for descent from 300 to 500 hPa ($\approx$ 3–4 km), corresponding to ≈ 0.12–0.16 km day^{-1}. This behavior is physically expected, due to increasing atmospheric stratification with height, as well as other factors such as the decline in radiative cooling rates above $\approx$ 200–250 hPa (e.g., Hartmann et al., 2022). Among the factors tested, the height of the source region emerges as the dominant control on transport timescales.

https://doi.org/10.5194/egusphere-2025-4338
Preprint. Discussion started: 14 January 2026

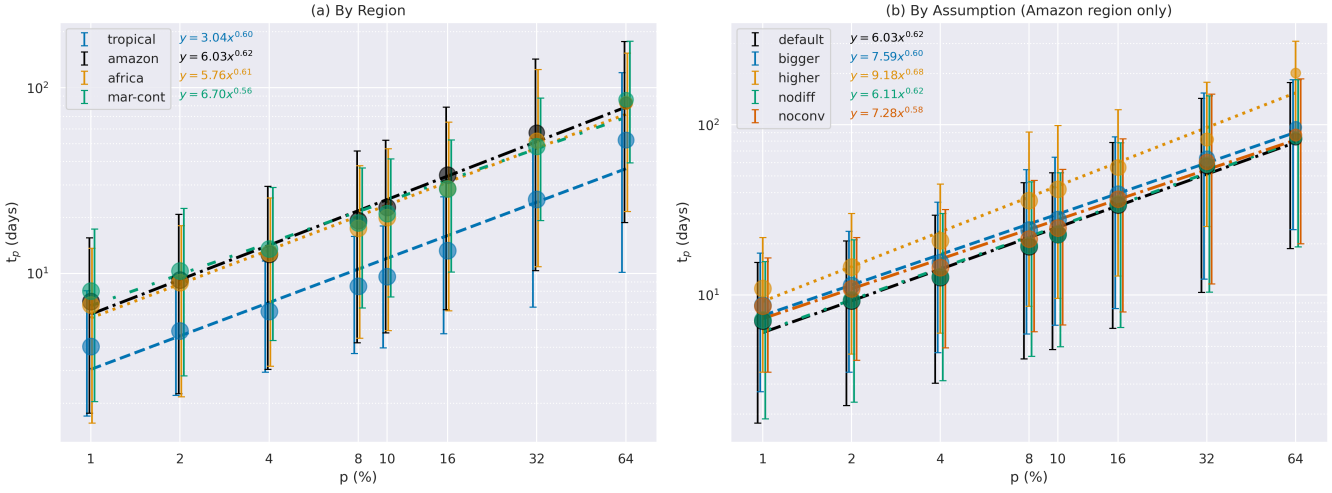

Figure 4. Time-to-threshold t_p at 500 hPa, inside the outer red polygons in Fig. 3, for varying thresholds. (a) Different regional tracers in the control run, and (b) Amazon regional tracer from different sensitivity experiments. Markers represent area averages, and the error bars indicate the interval between the 10^{th} and 90^{th} percentiles of t_p. Grid points where the threshold p is never reached by the end of the simulation are excluded. Marker size is proportional to the number of valid grid points. The straight lines illustrate power-law fits obtained via linear regression in log–log space, applied to the valid data points. The fitted parameters (slope and intercept) are shown in the upper-left corner, with text color matching the corresponding lines.

3.2 Patterns in the transport of regional tracers with sinks

In Section 3.1, we showed that the spatial patterns in downward transport timescales from the regional sources were consistent with those derived from the Tropical tracer, albeit with a scale factor difference due to the enhanced dilution associated with the smaller size of the source region. Given this consistency and the hypothesized greater potential for secondary aerosol nucleation in the UT over continental compared to maritime tropical regions, we focus on the regional tracer sources in this section. Here, 10-year statistics from the Amazon, Africa, and Maritime Continent constant tracers with sinks are used to provide a proxy for the background number mixing ratio in the mid-troposphere, assuming tropical, continental, UT sources under the influence of transport, wet scavenging, dry deposition, and sedimentation.

Overall, the distribution of $N_{\text{cnt}}/N_{\text{ref}}$ resembles the spatial patterns in the transport timescales discussed in Section 3.1. Figure 5a shows that the highest values of $N_{\text{cnt}}/N_{\text{ref}}$ from the regional tracers are found below and slightly shifted to the east of the source region –except for the mar-cont tracer, for which the maximum lies slightly southwest– where the downward transport from the regional sources is fastest (compare with Fig. 2 and 3). Values of $N_{\text{cnt}}/N_{\text{ref}}$ reaching ≈ 0.4 over northeastern South America and eastern Sub-Saharan Africa contrast with values generally less than 0.2 over the Maritime Continent (Fig. 5a), indicating more efficient downward transport from the Amazon and Africa source regions than from the Maritime Continent overall. The time-averaged equatorial cross section of the sum of the three regional tracers (Fig. 5b) shows that transport from the Maritime Continent exhibits a slightly predominant westward component, in contrast to the mainly eastward

https://doi.org/10.5194/egusphere-2025-4338
Preprint. Discussion started: 14 January 2026

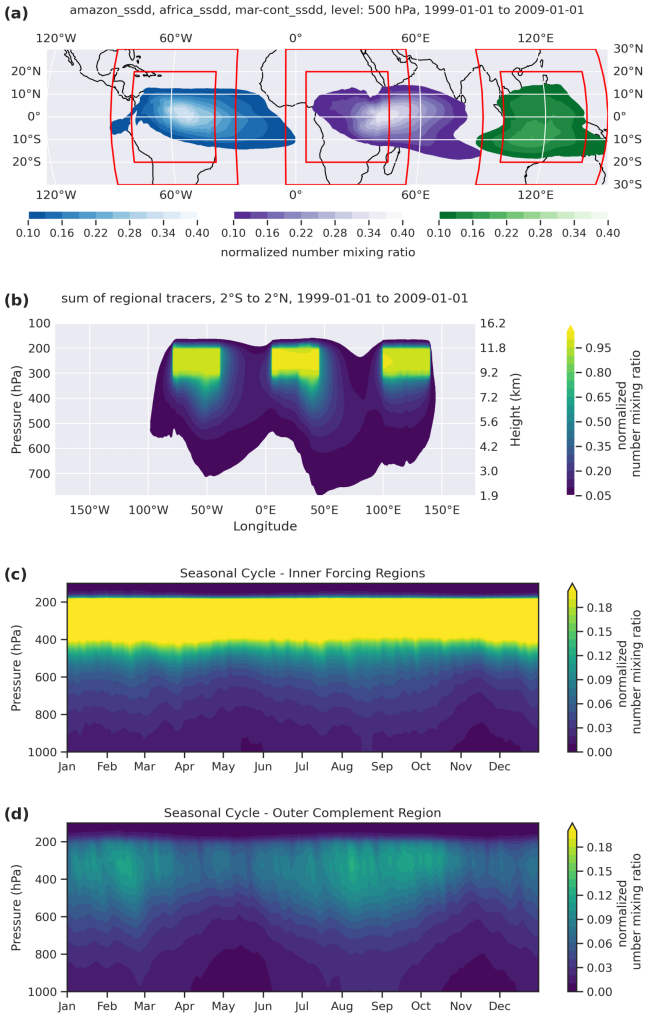

Figure 5. Spatial distribution and seasonality of the tracers amazon_constant_with_ssdd, africa_constant_with_ssdd, and mar-cont_constant_with_ssdd. a) Time-averaged normalized number mixing ratios $N_{\mathrm{cnt}}/N_{\mathrm{ref}}$ at 500 hPa; b) Cross-section of the time-averaged sum of the three tracers' number mixing ratios near the Equator ($\phi \pm 2^{\circ}$); c) Multi-year daily average of area-averaged vertical profiles of the sum of the three tracers' number mixing ratios at and below the forcing regions; d) Same as in (c), but between $\phi \pm 20^{\circ}$, excluding the forcing region areas. All time averages are computed over the simulation period from January 1, 1999 to December 1, 2008. Red rectangles in panel (a) indicate the forcing and averaging regions as in Fig. 2, for reference.

transport from the other two regions. This pattern likely reflects regional inhomogeneities in equatorial circulation, including the influence of the Tropical Easterly Jet (Chen and van Loon, 1987) and stronger divergence associated with deep convection (Trenberth et al., 2000), which may lead to partial compensation between eastward and westward transport in the time averages.

https://doi.org/10.5194/egusphere-2025-4338
Preprint. Discussion started: 14 January 2026

Figures 5c,d illustrate the seasonal variation of the area-averaged vertical profiles right below the forcing regions and outside of them, respectively. This shows that downward transport from the source regions to the mid-troposphere is sustained year-round, with $N_{\mathrm{cnt}}/N_{\mathrm{ref}}$ in the order of ≈ 0.1–0.15 on average at ≈ 500 hPa. Values of $N_{\mathrm{cnt}}/N_{\mathrm{ref}}$ in the mid-troposphere are higher from around January to March and July to October, with seasonal variations being more pronounced for columns in the outer complement region. This seasonality pattern is consistent with the north-south shifts of the ITCZ. The northern and southern extremes of the forcing region may be more easily embedded in the subsidence branch of the Hadley Cell during the local winter, as the ITCZ moves toward the summer hemisphere, accelerating downward transport compared to the local summer.

4 Discussion

The results presented in Section 3 provide a comprehensive view of the timescales, spatial pathways, and dilution effects associated with the vertical transport of tracers from tropical, UT source regions to the mid-troposphere, analyzed from an Eulerian global-model perspective.

Several robust patterns emerge from the analysis, with important implications for our understanding of aerosol transport in the tropical UT to mid-troposphere. First, the distinction between tropical-wide and regional tracer sources highlights the sensitivity of transport timescales to the spatial extent of the emission region (Figs. 1). The regional tracers exhibit significantly longer mean ages of air ($\langle\tau\rangle \approx 260$ days) than their tropical counterpart ($\langle\tau\rangle \approx 45$ days). This fivefold increase underscores the strong role of mixing and dilution when tracer release is geographically constrained, consistent with expectations from transport theory. A parallel can be drawn to previous variability-lifetime studies, which show that tracer spatial variability – and, by analogy, average age – is sensitive not only to residence time but also to the spatial distribution of sources and sinks (e.g., Bolin and Rodhe, 1973; Hamrud, 1983; Ott, 1990; Jobson et al., 1999). In general, enhanced widening of the age spectrum in the troposphere is expected, as it is linked to strong mixing in this layer. This contrasts with stratospheric conditions, where spatial variability is more strongly governed by residence time (Jobson et al., 1999), and the age-of-air approach is more straightforwardly applicable (e.g., Hall and Plumb, 1994; Waugh and Hall, 2002), owing to the strong stratification that limits vertical exchanges compared to the troposphere.

In the context analyzed here, the time-to-threshold diagnostic, particularly at the 10% level, provides a valuable complement to the mean age of air by capturing the onset of tracer influence in a given target region, effectively representing the left tail of the age spectrum. The broadly similar spatial patterns between these two diagnostics (Figs. 2 and 3) affirm the robustness of the large-scale subsidence pathways, while the shorter timescales (often < 7 days) highlight the potential for relatively rapid vertical connections to the mid-troposphere.

Although not explicitly shown here, these results imply that aerosol transport from the UT to even lower levels – such as the atmospheric boundary layer, where low and convective clouds typically form – would require significantly longer than one week if governed solely by resolved-scale advection. Therefore, while Zhao et al. (2020) reported consistent downward fluxes from the Amazonian UT to the boundary layer during their week-long simulations, such cross-troposphere connections are

https://doi.org/10.5194/egusphere-2025-4338
Preprint. Discussion started: 14 January 2026

unlikely to occur within that short timescale, unless faster mechanisms – such as convective downdrafts, which specific role has in this context has not been fully elucidated – come into play.

Among all sensitivity experiments, the height of the tracer release emerges as the dominant factor controlling descent times. An upward shift of 50 hPa of the source region (from 200–300 hPa to 150–250 hPa) increases $t_{10\%}$ by ≈ 19 days, pointing to nonlinear behavior, presumably governed by factors such as the vertical profile of stratification and radiative cooling rates. In contrast, the influence of particle size, convection and turbulence in our simulations is modest. Increasing the mean particle radius to 100 nm, leads to a $\approx 22\%$ increase in descent time, mostly due to relatively enhanced wet scavenging. In turn, neglecting convective transport results in a $\approx 10\%$ increase in descent time, while removing turbulent diffusion yields a minor delay of only $\approx 1\%$ (Fig. 4b). These results indicate that large-scale advection (and implicit diffusivity) dominates the mean transport from the UT to the mid-troposphere at 500 hPa, at least on regional and climatological scales.

The spatial structure of the constant-tracer number mixing ratios N_{cnt} under the combined influence of transport and sinks (Fig. 5) reinforces these conclusions. Regional tracers with constant sources and sinks dominated by wet scavenging exhibit peak mid-tropospheric number mixing ratios just east of their source regions – and slightly southwest in the case of the Maritime Continent tracer – aligning with the pattern of minimum transport times. This suggests a partial decoupling between the upper tropospheric source regions and the locations of fastest mid-tropospheric descent, consistent with the short-term simulations of Wang et al. (2023), which showed that aerosols entering the boundary layer over the Amazon often originated outside the region. Nonetheless, the duration of their simulation represents an important constraint on the generality of their results. Our findings indicate that, despite the tilted descent path over the Amazon, significant downward transport may still occur within the Amazon region – i.e., within the domain simulated by Wang et al. (2023) – provided the transport timescale exceeds one week.

The resulting largely zonal distribution of tracer mixing ratios and transit times found here is broadly consistent with the results of Merikanto et al. (2009), except that the tropical maxima reported in their study are not evident in our simulations. This difference likely arises from our constraint of the source region to latitudes between $\pm 20°$, whereas in Merikanto et al. (2009), the nucleation rate evolved freely in space, depending solely on precursor availability and environmental conditions.

The reduction in number mixing ratios from the UT to the mid-troposphere in our simulations is substantial, but values of $N_{\mathrm{cnt}}/N_{\mathrm{ref}} \approx 0.1$–$0.15$ remain meaningful and potentially important in the absence of other aerosol sources at lower altitudes. Notably, this fractional abundance is comparable to the contribution of secondary organic aerosols nucleated in the boundary layer relative to those formed in the upper troposphere in the numerical study of Zhu et al. (2019).

4.1 Estimated impact of coagulation

The absence of coagulation in our simulations represents a potentially important source of uncertainty in these estimates. To provide a rough assessment of the potential impact of coagulation, we integrated the coagulation equation over 7 days using a 1-min time step and a simple Euler integration method. Only Brownian coagulation was considered, using the kernel from Seinfeld and Pandis (2016, Table 13.1). A linear descent rate was assumed, implying linear variations in temperature and pressure over the intervals -50–$0\,°\mathrm{C}$ and 300–500 hPa, respectively. Particles were initially assumed to follow a log-normal

https://doi.org/10.5194/egusphere-2025-4338
Preprint. Discussion started: 14 January 2026

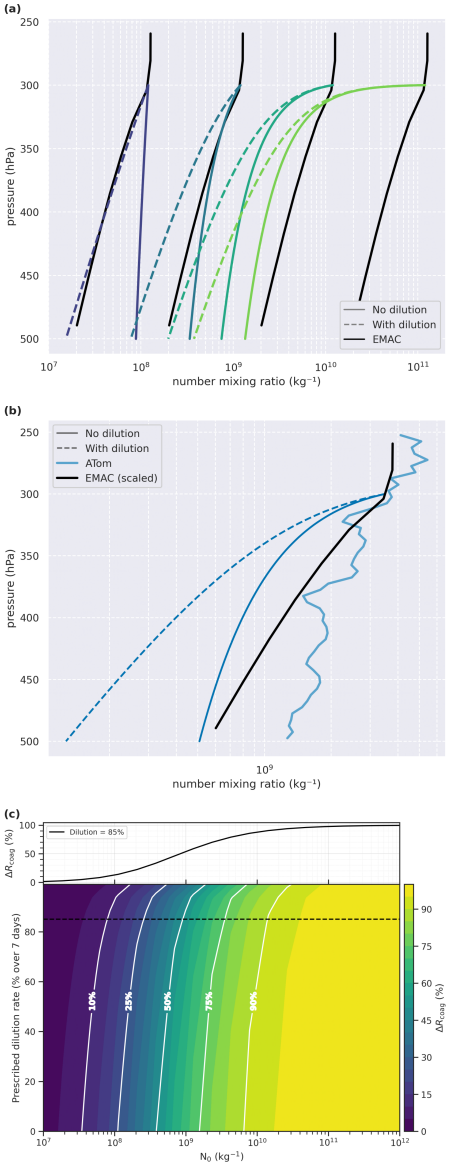

Figure 6. Theoretical impact of aerosol coagulation assuming linear descent and a prescribed dilution rate. a) Theoretical profiles along with scaled versions of the area-averaged number mixing ratio N_{cnt} below the forcing regions in the simulations. b) Similar to (a), but for the EMAC and theoretical coagulation profiles approximately matching the observed particle mixing ratios at 300 hPa from ATom 1 and 2 (limited to latitudes between $\pm 20°$), c) Excess reduction in number mixing ratio due to including coagulation besides dilution.

size distribution with a mean radius of 20 nm and a geometric standard deviation of 1.6, as in the EMAC simulations. The size distribution was discretized using a mass-doubling grid with 40 bins, starting from a minimum size edge of 0.47 nm. Based on the mean profile of the number mixing ratio N_{cnt}, derived from the sum of regional tracers at locations directly

https://doi.org/10.5194/egusphere-2025-4338
Preprint. Discussion started: 14 January 2026

below the forcing regions in 10 years of EMAC simulations (N_{EMAC}), an exponential decay was applied with an e-folding time of 3.69 days, corresponding to an 85% reduction in N_{cnt} over 7 days to represent the combined effects of dilution and wet scavenging.

The vertical profiles of number mixing ratio N for different initial values N_0, with and without the prescribed dilution rate, are shown in Fig. 6. In EMAC, the dominant processes affecting number mixing ratios are transport and wet scavenging, both of which act linearly on the number mixing ratio. As a result, the vertical gradient of the simulated tracer is preserved across different initial values, allowing for consistent scaling. We therefore include scaled versions of N_{EMAC} in Fig. 6a to facilitate comparison with the idealized profiles.

At high N_0, coagulation acts rapidly, producing substantial reductions in particle number early in the descent. This is evident in Figure 6a, where the calculations that include coagulation show much steeper initial decreases in N compared to EMAC, which accounts only for dilution, particularly for the larger values of N_0. The rapid initial loss reflects the N^2-dependence of the coagulation sink: the process is highly efficient when particle concentrations are large, but slows as N drops. When $N_0 \geq 10^{10}\,\mathrm{kg}^{-1}$ ($\approx 4680\,\mathrm{cm}^{-3}$ at a pressure of 300 hPa and a temperature of $-50\,^{\circ}\mathrm{C}$), coagulation dominates over the first ≈ 50 hPa of descent, beyond which dilution and mixing become the primary controls. At lower initial values –particularly $N_0 \leq 1.2 \times 10^9$ kg^{-1}, equivalent to $\approx 562\,\mathrm{cm}^{-3}$ at 300 hPa and$-50\,^{\circ}\mathrm{C}$, in Fig. 6a– the microphysical timescale becomes long compared to the transport timescale, and dilution alone governs most of the evolution.

Observations of tropical upper tropospheric (UT) aerosols typically fall within number mixing ratio ranges where coagulation is highly effective. This is illustrated by comparing the mean vertical profile of aerosol number mixing ratio from the Atmospheric Tomography Mission (ATom-1 and ATom-2, limited to latitudes between $\pm 20°$), reproduced from the dataset provided by Williamson et al. (2019), in Fig. 6b. However, the observed profile does not exhibit the steep vertical gradient predicted by the theoretical coagulation calculations presented here. Additional calculations (not shown) indicate that, for the coagulation profile to match the observations, an initial mean radius of approximately 100 nm at 300 hPa would be required. However, observations by Williamson et al. (2019) suggest that a mean radius of 20 nm is more representative of the natural particle size distributions at such altitudes, which are predominantly unimodal. Instead the observed profile more closely resembles the EMAC profile, which does not account for coagulation. This discrepancy is likely associated with a more vertically widespread distribution of aerosol sources in the real atmosphere, in contrast to the source-free evolution assumed in the idealized coagulation calculations. Nevertheless, for the theoretical investigation of UT particle evolution and the relative roles of transport and microphysical growth processes, the approach employed here remains useful.

To quantify the transition between the regime in which transport dominates and the one in which coagulation introduces significant variability, we compare the final number mixing ratio from the idealized coagulation-plus-dilution calculations to the theoretical value expected from dilution alone, assuming a constant dilution rate as in the EMAC mean profile in Fig. 6a. The excess reduction due to coagulation is defined as $\Delta R_{\mathrm{coag}} = (1 - N_{\mathrm{final,\,coag+dil}}/N_{\mathrm{final,\,dil}})100$, and is shown in Figure 6c as a function of initial N_0 and prescribed 7-day dilution rate. The excess remains below 50% for $N_0 \lesssim 4 \times 10^8$ kg^{-1}, and below 10% for $N_0 \lesssim 3 \times 10^7$ kg^{-1} at low dilution rates, and decreases monotonically as a function of the prescribed dilution. At the EMAC mean dilution rate (85%), $\Delta R_{\mathrm{coag}} \approx 50\%$ for $N_0 \approx 10^9$ kg^{-1}, and $\Delta R_{\mathrm{coag}} \approx 10\%$ for $N_0 \approx 6 \times 10^7$ kg^{-1}. This

https://doi.org/10.5194/egusphere-2025-4338
Preprint. Discussion started: 14 January 2026

identifies a regime in which the omission of coagulation is not expected to significantly bias tracer-based diagnostics. Figure 6 thus provides a physical basis for assessing and scaling potential errors introduced by the absence of coagulation in the EMAC simulations presented here, depending on the value of N_0 assumed.

Future studies should further explore several key processes and sensitivities that remain unresolved in the present analysis. In particular, the role of convective clouds in transporting aerosols from the UT downward remains uncertain. Higher-resolution simulations will be necessary to explicitly capture subsidence around convective cores and downdrafts from mature convection, which may locally accelerate vertical transport. Additionally, incorporating a seasonal migration of the aerosol source region accompanying the Intertropical Convergence Zone (ITCZ) and the impact of interannual variability such as ENSO could reveal important modulations of transport pathways and aerosol residence times. A more complete representation of aerosol lifecycle processes –including nucleation, condensational and coagulation growth, and wet removal of both, cloud particles and condensable vapors – would also improve estimates of aerosol number and transformations during descent. A follow-up study will incorporate these additional layers of complexity to better quantify the coupled dynamics-microphysics of aerosol transport from UT sources.

Finally, we include a brief note on the choice of Lagrangian versus Eulerian techniques. Lagrangian methods, including back/forward trajectories and particle–dispersion models, are widely used to characterize transport pathways and source attribution (e.g., Lin et al., 2003; Stohl et al., 2005; Stein et al., 2015; Sprenger and Wernli, 2015). One of their key advantages is the reduction of numerical diffusion compared to Eulerian models, which allows for better representation of gradients in tracer fields. However, they also face several limitations: results depend on sampling density; turbulent mixing and irreversible entrainment/detrainment are difficult to represent; vertical exchanges into and out of air parcels, including sedimentation and wet scavenging with possible re-evaporation, are challenging to treat along individual trajectories; and inferred ages and pathways remain sensitive to uncertainties in the wind fields driving them (Lin et al., 2012). Therefore, Eulerian and Lagrangian approaches remain complementary for identifying transport pathways and for case-specific process studies, the Lagrangian tracking component will be considered in future work.

5 Conclusions

This study provides a detailed assessment of vertical transport timescales, dilution, and spatial distribution of aerosol tracers released from tropical and tropical-continental UT source regions based on large-scale transport mechanisms. The key findings are:

- Transport timescales are highly sensitive to the extent of the source region. Regional continental tracers exhibit mean air ages of ≈ 260 days at 500 hPa, compared to ≈ 45 days for tropical-wide sources, highlighting the strong role of mixing and dilution for spatially confined emissions.
- While the mean age responds to the full distribution of transport pathways, the time-to-threshold diagnostic isolates the fastest transport. The two differ in sensitivity to source region size, with time-to-threshold varying by a factor of ≈ 2,

https://doi.org/10.5194/egusphere-2025-4338
Preprint. Discussion started: 14 January 2026

and mean age by a factor of ≈ 5. Importantly, timescales faster than 7 days were found for all source regions when considering the time to reach a 10% threshold, underscoring the efficiency of fast subsidence pathways.

- Descent time is strongly influenced by injection height. A 50 hPa increase in release altitude (from 200–300 hPa to 150–250 hPa) extends the time to reach the 10% threshold around the Amazon source region by approximately 19 days beyond the control case average (≈ 25 days), indicating a nonlinear sensitivity to source height.

- Large-scale advection dominates over parameterized convection and turbulent diffusion. Removing parameterized convective transport increases descent time by only $\approx 10\%$, while neglecting parameterized vertical diffusion has a negligible effect ($\approx 1\%$), indicating the primacy of large-scale circulation at the simulated scales.

- Mid-tropospheric maxima in tracer number mixing ratios appear east of the source region centers –except for the Maritime Continent tracer, which peaks slightly to the southwest–consistent with regional wind patterns. Despite substantial reduction, number mixing ratios on the order of 10–15% of the source region average remain potentially important.

- Overall, the vertical gradient of number mixing ratio simulated here is, in principle, independent of the values in the forcing region, due to the assumed linearity of transport and wet scavenging. However, these trends hold strictly only for low number mixing ratios, where coagulation effects are negligible. The estimated correction due to coagulation to the fraction of the source region's number mixing ratio reaching the mid-troposphere in our simulations is less than 10% when the initial assumed number mixing ratio is below approximately 6×10^7 kg^{-1}. Correction estimates as a function of number mixing ratio and dilution rate are provided.

Code and data availability. The Modular Earth Submodel System (MESSy) is being continuously further developed and applied by a consortium of institutions. The usage of MESSy and access to the source code is licenced to all affiliates of institutions who are members of the MESSy Consortium. Institutions can become a member of the MESSy Consortium by signing the MESSy Memorandum of Understanding. More information can be found on the MESSy Consortium website (http://www.messy-interface.org). The model version applied for the presented analyses is https://doi.org/10.5281/zenodo.17052244.

Author contributions. AP conceived the study. LHP, AP, JC, and PJ co-designed the model experiments. LHP carried out the simulations, performed all analyses, and wrote the manuscript. MM supported the model setup. All authors contributed to the editing of the manuscript and provided feedback on the analysis and its interpretation.

Competing interests. Two co-authors of the manuscript are topical editors of the journal.

https://doi.org/10.5194/egusphere-2025-4338
Preprint. Discussion started: 14 January 2026

Acknowledgements. The authors thank Holger Tost for the discussions on the simulation design and Astrid Kerkweg for the technical support. We thank Martin Heinritzi for his valuable comments on unpublished observational results. This work was funded by the Deutsche Forschungsgemeinschaft (DFG, German Research Foundation) - TRR 301 - Project-ID 428312742. This work used resources of the Deutsches Klimarechenzentrum (DKRZ) granted by its Scientific Steering Committee (WLA) under project ID bb1311. Further, datasets (MESSy initial and boundary conditions) provided by project pd1279 via the DKRZ data pool were used. AI has been used for grammar and scripting support.

https://doi.org/10.5194/egusphere-2025-4338
Preprint. Discussion started: 14 January 2026

References

Andreae, M. O., Afchine, A., Albrecht, R., Holanda, B. A., Artaxo, P., Barbosa, H. M. J., Borrmann, S., Cecchini, M. A., Costa, A., Dollner, M., Fütterer, D., Järvinen, E., Jurkat, T., Klimach, T., Konemann, T., Knote, C., Krämer, M., Krisna, T., Machado, L. A. T., Mertes, S., Minikin, A., Pöhlker, C., Pöhlker, M. L., Pöschl, U., Rosenfeld, D., Sauer, D., Schlager, H., Schnaiter, M., Schneider, J., Schulz, C., Spanu, A., Sperling, V. B., Voigt, C., Walser, A., Wang, J., Weinzierl, B., Wendisch, M., and Ziereis, H.: Aerosol characteristics and particle production in the upper troposphere over the Amazon Basin, Atmospheric Chemistry and Physics, 18, 921–961, https://doi.org/10.5194/acp-18-921-2018, 2018.

Asselin, R.: Frequency Filter for Time Integrations, Monthly Weather Review, 100, 487 – 490, https://doi.org/10.1175/1520-0493(1972)100<0487:FFFTI>2.3.CO;2, 1972.

Bolin, B. and Rodhe, H.: A note on the concepts of age distribution and transit time in natural reservoirs, Tellus, 25, 58–62, https://doi.org/https://doi.org/10.1111/j.2153-3490.1973.tb01594.x, 1973.

Brewer, A. W.: Evidence for a world circulation provided by the measurements of helium and water vapour distribution in the stratosphere, Quarterly Journal of the Royal Meteorological Society, 75, 351–363, https://doi.org/https://doi.org/10.1002/qj.49707532603, 1949.

Brock, C. A., Hamill, P., Wilson, J. C., Jonsson, H. H., and Chan, K. R.: Particle Formation in the Upper Tropical Troposphere: A Source of Nuclei for the Stratospheric Aerosol, Science, 270, 1650–1653, https://doi.org/10.1126/science.270.5242.1650, 1995.

Burridge, D. M. and Haseler, J.: A model for medium range weather forecasting - Adiabatic formulation, Tech. rep., 1977.

Chen, T.-C. and van Loon, H.: Interannual Variation of the Tropical Easterly Jet, Monthly Weather Review, 115, 1739 – 1759, https://doi.org/10.1175/1520-0493(1987)115<1739:IVOTTE>2.0.CO;2, 1987.

Clarke, A. D.: Atmospheric nuclei in the Pacific midtroposphere: Their nature, concentration, and evolution, Journal of Geophysical Research: Atmospheres, 98, 20 633–20 647, https://doi.org/https://doi.org/10.1029/93JD00797, 1993.

Clarke, A. D. and Kapustin, V. N.: A Pacific Aerosol Survey. Part I: A Decade of Data on Particle Production, Transport, Evolution, and Mixing in the Troposphere, Journal of the Atmospheric Sciences, 59, 363 – 382, https://doi.org/10.1175/1520-0469(2002)059<0363:APASPI>2.0.CO;2, 2002.

Clarke, A. D., Varner, J. L., Eisele, F., Mauldin, R. L., Tanner, D., and Litchy, M.: Particle production in the remote marine atmosphere: Cloud outflow and subsidence during ACE 1, Journal of Geophysical Research: Atmospheres, 103, 16 397–16 409, https://doi.org/https://doi.org/10.1029/97JD02987, 1998.

Clarke, A. D., Eisele, F., Kapustin, V. N., Moore, K., Tanner, D., Mauldin, L., Litchy, M., Lienert, B., Carroll, M. A., and Albercook, G.: Nucleation in the equatorial free troposphere: Favorable environments during PEM-Tropics, Journal of Geophysical Research: Atmospheres, 104, 5735–5744, https://doi.org/https://doi.org/10.1029/98JD02303, 1999.

Covert, D. S., Kapustin, V. N., Bates, T. S., and Quinn, P. K.: Physical properties of marine boundary layer aerosol particles of the mid-Pacific in relation to sources and meteorological transport, Journal of Geophysical Research: Atmospheres, 101, 6919–6930, https://doi.org/https://doi.org/10.1029/95JD03068, 1996.

Curtius, J., Heinritzi, M., Beck, L. J., Pöhlker, M. L., Tripathi, N., Krumm, B. E., Holzbeck, P., Nussbaumer, C. M., Pardo, L. H., Klimach, T., Barmpounis, K., Andersen, S. T., Bardakov, R., Bohn, B., Cecchini, M. A., Chaboureau, J.-P., Dauhut, T., Dienhart, D., Dörich, R., Edtbauer, A., Giez, A., Hartmann, A., Holanda, B. A., Joppe, P., Kaiser, K., Keber, T., Klebach, H., Krüger, O. O., Kürten, A., Mallaun, C., Marno, D., Martinez, M., Monteiro, C., Nelson, C., Ort, L., Raj, S. S., Richter, S., Ringsdorf, A., Rocha, F., Simon, M., Sreekumar, S., Tsokankunku, A., Unfer, G. R., Valenti, I. D., Wang, N., Zahn, A., Zauner-Wieczorek, M., Albrecht, R. I., Andreae, M. O., Artaxo,

https://doi.org/10.5194/egusphere-2025-4338
Preprint. Discussion started: 14 January 2026

P., Crowley, J. N., Fischer, H., Harder, H., Herdies, D. L., Machado, L. A. T., Pöhlker, C., Pöschl, U., Possner, A., Pozzer, A., Schneider, J., Williams, J., and Lelieveld, J.: Isoprene nitrates drive new particle formation in Amazon's upper troposphere, Nature, 636, 124—-130, https://doi.org/10.1038/s41586-024-08192-4, 2024.

de Reus, M., Krejci, R., Williams, J., Fischer, H., Scheele, R., and Ström, J.: Vertical and horizontal distributions of the aerosol number concentration and size distribution over the northern Indian Ocean, Journal of Geophysical Research: Atmospheres, 106, 28 629–28 641, https://doi.org/https://doi.org/10.1029/2001JD900017, 2001.

Dietmüller, S., Jöckel, P., Tost, H., Kunze, M., Gellhorn, C., Brinkop, S., Frömming, C., Ponater, M., Steil, B., Lauer, A., and Hendricks, J.: A new radiation infrastructure for the Modular Earth Submodel System (MESSy, based on version 2.51), Geoscientific Model Development, 9, 2209–2222, https://doi.org/10.5194/gmd-9-2209-2016, 2016.

Dobson, G. M. B. and Massey, H. S. W.: Origin and distribution of the polyatomic molecules in the atmosphere, Proceedings of the Royal Society of London. Series A. Mathematical and Physical Sciences, 236, 187–193, https://doi.org/10.1098/rspa.1956.0127, 1956.

Ekman, A. M. L., Hermann, M., Groß, P., Heintzenberg, J., Kim, D., and Wang, C.: Sub-micrometer aerosol particles in the upper troposphere/lowermost stratosphere as measured by CARIBIC and modeled using the MIT-CAM3 global climate model, Journal of Geophysical Research: Atmospheres, 117, https://doi.org/https://doi.org/10.1029/2011JD016777, 2012.

Emmerichs, T., Kerkweg, A., Ouwersloot, H., Fares, S., Mammarella, I., and Taraborrelli, D.: A revised dry deposition scheme for land–atmosphere exchange of trace gases in ECHAM/MESSy v2.54, Geoscientific Model Development, 14, 495–519, https://doi.org/10.5194/gmd-14-495-2021, 2021.

English, J. M., Toon, O. B., Mills, M. J., and Yu, F.: Microphysical simulations of new particle formation in the upper troposphere and lower stratosphere, Atmospheric Chemistry and Physics, 11, 9303–9322, https://doi.org/10.5194/acp-11-9303-2011, 2011.

Franco, M. A., Ditas, F., Kremper, L. A., Machado, L. A. T., Andreae, M. O., Araújo, A., Barbosa, H. M. J., de Brito, J. F., Carbone, S., Holanda, B. A., Morais, F. G., Nascimento, J. P., Pöhlker, M. L., Rizzo, L. V., Sá, M., Saturno, J., Walter, D., Wolff, S., Pöschl, U., Artaxo, P., and Pöhlker, C.: Occurrence and growth of sub-50 nm aerosol particles in the Amazonian boundary layer, Atmospheric Chemistry and Physics Discussions, 2021, 1–36, https://doi.org/10.5194/acp-2021-765, 2021.

Froyd, K. D., Murphy, D. M., Sanford, T. J., Thomson, D. S., Wilson, J. C., Pfister, L., and Lait, L.: Aerosol composition of the tropical upper troposphere, Atmospheric Chemistry and Physics, 9, 4363–4385, https://doi.org/10.5194/acp-9-4363-2009, 2009.

Hall, T. M. and Plumb, R. A.: Age as a diagnostic of stratospheric transport, Journal of Geophysical Research: Atmospheres, 99, 1059–1070, https://doi.org/https://doi.org/10.1029/93JD03192, 1994.

Hamill, P., Jensen, E. J., Russell, P. B., and Bauman, J. J.: The Life Cycle of Stratospheric Aerosol Particles, Bulletin of the American Meteorological Society, 78, 1395 – 1410, https://doi.org/10.1175/1520-0477(1997)078<1395:TLCOSA>2.0.CO;2, 1997.

Hamrud, M.: Residence time and spatial variability for gases in the atmosphere, Tellus B: Chemical and Physical Meteorology, 35, 295–303, https://doi.org/10.3402/tellusb.v35i5.14619, 1983.

Hartmann, D. L., Dygert, B. D., Blossey, P. N., Fu, Q., and Sokol, A. B.: The Vertical Profile of Radiative Cooling and Lapse Rate in a Warming Climate, Journal of Climate, 35, 6253 – 6265, https://doi.org/10.1175/JCLI-D-21-0861.1, 2022.

Heintzenberg, J., Hermann, M., Weigelt, A., Clarke, A., Kapustin, V., Anderson, B., Thornhill, K., Velthoven, P. V., Zahn, A., and Brenninkmeijer, C.: Near-global aerosol mapping in the upper troposphere and lowermost stratosphere with data from the CARIBIC project, Tellus B: Chemical and Physical Meteorology, 63, 875–890, https://doi.org/10.1111/j.1600-0889.2011.00578.x, 2011.

Hersbach, H., Bell, B., Berrisford, P., Hirahara, S., Horányi, A., Muñoz-Sabater, J., Nicolas, J., Peubey, C., Radu, R., Schepers, D., Simmons, A., Soci, C., Abdalla, S., Abellan, X., Balsamo, G., Bechtold, P., Biavati, G., Bidlot, J., Bonavita, M., De Chiara, G., Dahlgren,

https://doi.org/10.5194/egusphere-2025-4338
Preprint. Discussion started: 14 January 2026

P., Dee, D., Diamantakis, M., Dragani, R., Flemming, J., Forbes, R., Fuentes, M., Geer, A., Haimberger, L., Healy, S., Hogan, R. J., Hólm, E., Janisková, M., Keeley, S., Laloyaux, P., Lopez, P., Lupu, C., Radnoti, G., de Rosnay, P., Rozum, I., Vamborg, F., Villaume, S., and Thépaut, J.-N.: The ERA5 global reanalysis, Quarterly Journal of the Royal Meteorological Society, 146, 1999–2049, https://doi.org/https://doi.org/10.1002/qj.3803, 2020.

Jobson, B. T., McKeen, S. A., Parrish, D. D., Fehsenfeld, F. C., Blake, D. R., Goldstein, A. H., Schauffler, S. M., and Elkins, J. W.: Trace gas mixing ratio variability versus lifetime in the troposphere and stratosphere: Observations, Journal of Geophysical Research: Atmospheres, 104, 16 091–16 113, https://doi.org/https://doi.org/10.1029/1999JD900126, 1999.

Jöckel, P., Sander, R., Kerkweg, A., Tost, H., and Lelieveld, J.: Technical Note: The Modular Earth Submodel System (MESSy) - a new approach towards Earth System Modeling, Atmospheric Chemistry and Physics, 5, 433–444, https://doi.org/10.5194/acp-5-433-2005, 2005.

Jöckel, P., Tost, H., Pozzer, A., Brühl, C., Buchholz, J., Ganzeveld, L., Hoor, P., Kerkweg, A., Lawrence, M. G., Sander, R., Steil, B., Stiller, G., Tanarhte, M., Taraborrelli, D., van Aardenne, J., and Lelieveld, J.: The atmospheric chemistry general circulation model ECHAM5/MESSy1: consistent simulation of ozone from the surface to the mesosphere, Atmospheric Chemistry and Physics, 6, 5067–5104, https://doi.org/10.5194/acp-6-5067-2006, 2006.

Jöckel, P., Kerkweg, A., Buchholz-Dietsch, J., Tost, H., Sander, R., and Pozzer, A.: Technical Note: Coupling of chemical processes with the Modular Earth Submodel System (MESSy) submodel TRACER, Atmospheric Chemistry and Physics, 8, 1677–1687, https://doi.org/10.5194/acp-8-1677-2008, 2008.

Jöckel, P., Kerkweg, A., Pozzer, A., Sander, R., Tost, H., Riede, H., Baumgaertner, A., Gromov, S., and Kern, B.: Development cycle 2 of the Modular Earth Submodel System (MESSy2), Geoscientific Model Development, 3, 717–752, https://doi.org/10.5194/gmd-3-717-2010, 2010.

Kerkweg, A. and Jöckel, P.: The infrastructure MESSy submodels GRID (v1.0) and IMPORT (v1.0), Geoscientific Model Development Discussions, 8, 8607–8633, https://doi.org/10.5194/gmdd-8-8607-2015, 2015.

Kerkweg, A., Buchholz, J., Ganzeveld, L., Pozzer, A., Tost, H., and Jöckel, P.: Technical Note: An implementation of the dry removal processes DRY DEPosition and SEDImentation in the Modular Earth Submodel System (MESSy), Atmospheric Chemistry and Physics, 6, 4617–4632, https://doi.org/10.5194/acp-6-4617-2006, 2006a.

Kerkweg, A., Sander, R., Tost, H., and Jöckel, P.: Technical note: Implementation of prescribed (OFFLEM), calculated (ONLEM), and pseudo-emissions (TNUDGE) of chemical species in the Modular Earth Submodel System (MESSy), Atmospheric Chemistry and Physics, 6, 3603–3609, https://doi.org/10.5194/acp-6-3603-2006, 2006b.

Lampilahti, J., Leino, K., Manninen, A., Poutanen, P., Franck, A., Peltola, M., Hietala, P., Beck, L., Dada, L., Quéléver, L., Öhrnberg, R., Zhou, Y., Ekblom, M., Vakkari, V., Zilitinkevich, S., Kerminen, V.-M., Petäjä, T., and Kulmala, M.: Aerosol particle formation in the upper residual layer, Atmospheric Chemistry and Physics, 21, 7901–7915, https://doi.org/10.5194/acp-21-7901-2021, 2021.

Lee, S.-H., Reeves, J. M., Wilson, J. C., Hunton, D. E., Viggiano, A. A., Miller, T. M., Ballenthin, J. O., and Lait, L. R.: Particle Formation by Ion Nucleation in the Upper Troposphere and Lower Stratosphere, Science, 301, 1886–1889, https://doi.org/10.1126/science.1087236, 2003.

Lin, J., Brunner, D., Gerbig, C., Stohl, A., Luhar, A., and Webley, P., eds.: Lagrangian Modeling of the Atmosphere, vol. 200 of *Geophysical Monograph Series*, American Geophysical Union, Washington, D.C., ISBN 9781118704578, https://doi.org/10.1029/GM200, 2012.

https://doi.org/10.5194/egusphere-2025-4338
Preprint. Discussion started: 14 January 2026

Lin, J. C., Gerbig, C., Wofsy, S. C., Andrews, A. E., Daube, B. C., Davis, K. J., and Grainger, C. A.: A near-field tool for simulating the upstream influence of atmospheric observations: The Stochastic Time-Inverted Lagrangian Transport (STILT) model, Journal of Geophysical Research: Atmospheres, 108, https://doi.org/https://doi.org/10.1029/2002JD003161, 2003.

Lin, S.-J. and Rood, R. B.: Multidimensional Flux-Form Semi-Lagrangian Transport Schemes, Monthly Weather Review, 124, 2046 – 2070, https://doi.org/10.1175/1520-0493(1996)124<2046:MFFSLT>2.0.CO;2, 1996.

Lohmann, U. and Roeckner, E.: Design and performance of a new cloud microphysics scheme developed for the ECHAM general circulation model, Climate Dynamics, 12, 557–572, https://doi.org/10.1007/BF00207939, 1996.

Lott, F.: Alleviation of Stationary Biases in a GCM through a Mountain Drag Parameterization Scheme and a Simple Representation of Mountain Lift Forces, Monthly Weather Review, 127, 788 – 801, https://doi.org/10.1175/1520-0493(1999)127%3C0788:AOSBIA%3E2.0.CO;2, 1999.

Lott, F. and Miller, M. J.: A new subgrid-scale orographic drag parametrization: Its formulation and testing, Quarterly Journal of the Royal Meteorological Society, 123, 101–127, https://doi.org/https://doi.org/10.1002/qj.49712353704, 1997.

Machado, L. A. T., Franco, M. A., Kremper, L. A., Ditas, F., Andreae, M. O., Artaxo, P., Cecchini, M. A., Holanda, B. A., Pöhlker, M. L., Saraiva, I., Wolff, S., Pöschl, U., and Pöhlker, C.: How weather events modify aerosol particle size distributions in the Amazon boundary layer, Atmospheric Chemistry and Physics, 21, 18 065–18 086, https://doi.org/10.5194/acp-21-18065-2021, 2021.

Mann, G. W., Carslaw, K. S., Ridley, D. A., Spracklen, D. V., Pringle, K. J., Merikanto, J., Korhonen, H., Schwarz, J. P., Lee, L. A., Manktelow, P. T., Woodhouse, M. T., Schmidt, A., Breider, T. J., Emmerson, K. M., Reddington, C. L., Chipperfield, M. P., and Pickering, S. J.: Intercomparison of modal and sectional aerosol microphysics representations within the same 3-D global chemical transport model, Atmospheric Chemistry and Physics, 12, 4449–4476, https://doi.org/10.5194/acp-12-4449-2012, 2012.

Mauritsen, T., Bader, J., Becker, T., Behrens, J., Bittner, M., Brokopf, R., Brovkin, V., Claussen, M., Crueger, T., Esch, M., Fast, I., Fiedler, S., Fläschner, D., Gayler, V., Giorgetta, M., Goll, D. S., Haak, H., Hagemann, S., Hedemann, C., Hohenegger, C., Ilyina, T., Jahns, T., Jimenéz-de-la Cuesta, D., Jungclaus, J., Kleinen, T., Kloster, S., Kracher, D., Kinne, S., Kleberg, D., Lasslop, G., Kornblueh, L., Marotzke, J., Matei, D., Meraner, K., Mikolajewicz, U., Modali, K., Möbis, B., Müller, W. A., Nabel, J. E. M. S., Nam, C. C. W., Notz, D., Nyawira, S.-S., Paulsen, H., Peters, K., Pincus, R., Pohlmann, H., Pongratz, J., Popp, M., Raddatz, T. J., Rast, S., Redler, R., Reick, C. H., Rohrschneider, T., Schemann, V., Schmidt, H., Schnur, R., Schulzweida, U., Six, K. D., Stein, L., Stemmler, I., Stevens, B., von Storch, J.-S., Tian, F., Voigt, A., Vrese, P., Wieners, K.-H., Wilkenskjeld, S., Winkler, A., and Roeckner, E.: Developments in the MPI-M Earth System Model version 1.2 (MPI-ESM1.2) and Its Response to Increasing CO2, Journal of Advances in Modeling Earth Systems, 11, 998–1038, https://doi.org/https://doi.org/10.1029/2018MS001400, 2019.

Merikanto, J., Spracklen, D. V., Mann, G. W., Pickering, S. J., and Carslaw, K. S.: Impact of nucleation on global CCN, Atmospheric Chemistry and Physics, 9, 8601–8616, https://doi.org/10.5194/acp-9-8601-2009, 2009.

Minikin, A., Petzold, A., Ström, J., Krejci, R., Seifert, M., van Velthoven, P., Schlager, H., and Schumann, U.: Aircraft observations of the upper tropospheric fine particle aerosol in the Northern and Southern Hemispheres at midlatitudes, Geophysical Research Letters, 30, https://doi.org/https://doi.org/10.1029/2002GL016458, 2003.

Müller, W. A., Jungclaus, J. H., Mauritsen, T., Baehr, J., Bittner, M., Budich, R., Bunzel, F., Esch, M., Ghosh, R., Haak, H., Ilyina, T., Kleine, T., Kornblueh, L., Li, H., Modali, K., Notz, D., Pohlmann, H., Roeckner, E., Stemmler, I., Tian, F., and Marotzke, J.: A Higher-resolution Version of the Max Planck Institute Earth System Model (MPI-ESM1.2-HR), Journal of Advances in Modeling Earth Systems, 10, 1383–1413, https://doi.org/https://doi.org/10.1029/2017MS001217, 2018.

https://doi.org/10.5194/egusphere-2025-4338
Preprint. Discussion started: 14 January 2026

Nilsson, E. D., Rannik, U., Kumala, M., Buzorius, G., and O'dowd, C. D.: Effects of continental boundary layer evolution, convection, turbulence and entrainment, on aerosol formation, Tellus B: Chemical and Physical Meteorology, 53, 441–461, https://doi.org/10.3402/tellusb.v53i4.16617, 2001.

Nordeng, T.-E.: Extended versions of the convective parametrization scheme at ECMWF and their impact on the mean and transient activity of the model in the tropics, https://doi.org/10.21957/e34xwhysw, 1994.

Ott, W. R.: A Physical Explanation of the Lognormality of Pollutant Concentrations, Journal of the Air & Waste Management Association, 40, 1378–1383, https://doi.org/10.1080/10473289.1990.10466789, 1990.

Podglajen, A. and Ploeger, F.: Retrieving the age of air spectrum from tracers: principle and method, Atmospheric Chemistry and Physics, 19, 1767–1783, https://doi.org/10.5194/acp-19-1767-2019, 2019.

Raes, F.: Entrainment of free tropospheric aerosols as a regulating mechanism for cloud condensation nuclei in the remote marine boundary layer, Journal of Geophysical Research: Atmospheres, 100, 2893–2903, https://doi.org/https://doi.org/10.1029/94JD02832, 1995.

Raes, F., Dingenen, R. V., Vignati, E., Wilson, J., Putaud, J.-P., Seinfeld, J. H., and Adams, P.: Formation and cycling of aerosols in the global troposphere, Atmospheric Environment, 34, 4215–4240, https://doi.org/https://doi.org/10.1016/S1352-2310(00)00239-9, 2000.

Robert, A.: A stable numerical integration scheme for the primitive meteorological equations, Atmosphere-Ocean, 19, 35–46, https://doi.org/10.1080/07055900.1981.9649098, 1981.

Robert, A.: A scheme that combines semi-ragrangene and semi-imprisit methods for primitive equations, Journal of the Meteorological Society of Japan. Ser. II, 60, 319–325, https://doi.org/10.2151/jmsj1965.60.1_319, 1982.

Robert, A., Henderson, J., and Turnbull, C.: An Implicit Time Integration Scheme for Baroclinic Models of the Atmosphere, Monthly Weather Review, 100, 329 – 335, https://doi.org/10.1175/1520-0493(1972)100<0329:AITISF>2.3.CO;2, 1972.

Roeckner, E., Bäuml, G., Bonaventura, L., Brokopf, R., Esch, M., Giorgetta, M., Hagemann, S., Kirchner, I., Kornblueh, L., Manzini, E., Rhodin, A., Schlese, U., Schulzweida, U., , and Tompkins, A.: The atmospheric general circulation model ECHAM 5. PART I: Model description, Tech. rep., https://doi.org/10.17617/2.995269, 2003.

Schupfner, M., Wieners, K.-H., Wachsmann, F., Milinski, S., Steger, C., Bittner, M., Jungclaus, J., Früh, B., Pankatz, K., Giorgetta, M., Reick, C., Legutke, S., Esch, M., Gayler, V., Haak, H., de Vrese, P., Raddatz, T., Mauritsen, T., von Storch, J.-S., Behrens, J., Brovkin, V., Claussen, M., Crueger, T., Fast, I., Fiedler, S., Hagemann, S., Hohenegger, C., Jahns, T., Kloster, S., Kinne, S., Lasslop, G., Kornblueh, L., Marotzke, J., Matei, D., Meraner, K., Mikolajewicz, U., Modali, K., Müller, W., Nabel, J., Notz, D., Peters-von Gehlen, K., Pincus, R., Pohlmann, H., Pongratz, J., Rast, S., Schmidt, H., Schnur, R., Schulzweida, U., Six, K., Stevens, B., Voigt, A., and Roeckner, E.: DKRZ MPI-ESM1.2-LR model output prepared for CMIP6 ScenarioMIP, 2023.

Seinfeld, J. H. and Pandis, S. N.: Atmospheric chemistry and physics: from air pollution to climate change, John Wiley & Sons, 2016.

Simmons, A. J. and Burridge, D. M.: An Energy and Angular-Momentum Conserving Vertical Finite-Difference Scheme and Hybrid Vertical Coordinates, Monthly Weather Review, 109, 758 – 766, https://doi.org/10.1175/1520-0493(1981)109<0758:AEAAMC>2.0.CO;2, 1981.

Sprenger, M. and Wernli, H.: The LAGRANTO Lagrangian analysis tool – version 2.0, Geoscientific Model Development, 8, 2569–2586, https://doi.org/10.5194/gmd-8-2569-2015, 2015.

Stein, A. F., Draxler, R. R., Rolph, G. D., Stunder, B. J. B., Cohen, M. D., and Ngan, F.: NOAA's HYSPLIT Atmospheric Transport and Dispersion Modeling System, Bulletin of the American Meteorological Society, 96, 2059 – 2077, https://doi.org/10.1175/BAMS-D-14-00110.1, 2015.

Stohl, A., Forster, C., Frank, A., Seibert, P., and Wotawa, G.: Technical note: The Lagrangian particle dispersion model FLEXPART version 6.2, Atmospheric Chemistry and Physics, 5, 2461–2474, https://doi.org/10.5194/acp-5-2461-2005, 2005.

https://doi.org/10.5194/egusphere-2025-4338
Preprint. Discussion started: 14 January 2026

Sundqvist, H.: A parameterization scheme for non-convective condensation including prediction of cloud water content, Quarterly Journal of the Royal Meteorological Society, 104, 677–690, https://doi.org/https://doi.org/10.1002/qj.49710444110, 1978.

Sundqvist, H., Berge, E., and Kristjánsson, J. E.: Condensation and Cloud Parameterization Studies with a Mesoscale Numerical Weather Prediction Model, Monthly Weather Review, 117, 1641 – 1657, https://doi.org/10.1175/1520-0493(1989)117<1641:CACPSW>2.0.CO;2, 1989.

Tiedtke, M.: A Comprehensive Mass Flux Scheme for Cumulus Parameterization in Large-Scale Models, Monthly Weather Review, 117, 1779 – 1800, https://doi.org/10.1175/1520-0493(1989)117<1779:ACMFSF>2.0.CO;2, 1989.

Tost, H., Jöckel, P., Kerkweg, A., Sander, R., and Lelieveld, J.: Technical note: A new comprehensive SCAVenging submodel for global atmospheric chemistry modelling, Atmospheric Chemistry and Physics, 6, 565–574, https://doi.org/10.5194/acp-6-565-2006, 2006.

Trenberth, K. E., Stepaniak, D. P., and Caron, J. M.: The Global Monsoon as Seen through the Divergent Atmospheric Circulation, Journal of Climate, 13, 3969 – 3993, https://doi.org/10.1175/1520-0442(2000)013<3969:TGMAST>2.0.CO;2, 2000.

Varanda Rizzo, L., Roldin, P., Brito, J., Backman, J., Swietlicki, E., Krejci, R., Tunved, P., Petäjä, T., Kulmala, M., and Artaxo, P.: Multi-year statistical and modeling analysis of submicrometer aerosol number size distributions at a rain forest site in Amazonia, Atmospheric Chemistry and Physics, 18, 10 255–10 274, https://doi.org/10.5194/acp-18-10255-2018, 2018.

Wang, J., Krejci, R., Giangrande, S., Kuang, C., Barbosa, H. M. J., Brito, J., Carbone, S., Chi, X., Comstock, J., Ditas, F., Lavric, J., Manninen, H. E., Mei, F., Moran-Zuloaga, D., Pöhlker, C., Pöhlker, M. L., Saturno, J., Schmid, B., Souza, R. A. F., Springston, S. R., Tomlinson, J. M., Toto, T., Walter, D., Wimmer, D., Smith, J. N., Kulmala, M., Machado, L. A. T., Artaxo, P., Andreae, M. O., Petäjä, T., and Martin, S. T.: Amazon boundary layer aerosol concentration sustained by vertical transport during rainfall, Nature, 539, 416–419, https://doi.org/10.1038/nature19819, 2016.

Wang, X., Gordon, H., Grosvenor, D. P., Andreae, M. O., and Carslaw, K. S.: Contribution of regional aerosol nucleation to low-level CCN in an Amazonian deep convective environment: results from a regionally nested global model, Atmospheric Chemistry and Physics, 23, 4431–4461, https://doi.org/10.5194/acp-23-4431-2023, 2023.

Watson-Parris, D., Schutgens, N., Reddington, C., Pringle, K. J., Liu, D., Allan, J. D., Coe, H., Carslaw, K. S., and Stier, P.: In situ constraints on the vertical distribution of global aerosol, Atmospheric Chemistry and Physics, 19, 11 765–11 790, https://doi.org/10.5194/acp-19-11765-2019, 2019.

Waugh, D. and Hall, T.: Age of stratospheric air: Theory, observations, and models, Reviews of Geophysics, 40, 1–1–1–26, https://doi.org/https://doi.org/10.1029/2000RG000101, 2002.

Weigel, R., Borrmann, S., Kazil, J., Minikin, A., Stohl, A., Wilson, J. C., Reeves, J. M., Kunkel, D., de Reus, M., Frey, W., Lovejoy, E. R., Volk, C. M., Viciani, S., D'Amato, F., Schiller, C., Peter, T., Schlager, H., Cairo, F., Law, K. S., Shur, G. N., Belyaev, G. V., and Curtius, J.: In situ observations of new particle formation in the tropical upper troposphere: the role of clouds and the nucleation mechanism, Atmospheric Chemistry and Physics, 11, 9983–10 010, https://doi.org/10.5194/acp-11-9983-2011, 2011.

Weigelt, A., Hermann, M., van Velthoven, P. F. J., Brenninkmeijer, C. A. M., Schlaf, G., Zahn, A., and Wiedensohler, A.: Influence of clouds on aerosol particle number concentrations in the upper troposphere, Journal of Geophysical Research: Atmospheres, 114, https://doi.org/https://doi.org/10.1029/2008JD009805, 2009.

Williamson, C. J., Kupc, A., Axisa, D., Bilsback, K. R., Bui, T., Campuzano-Jost, P., Dollner, M., Froyd, K. D., Hodshire, A. L., Jimenez, J. L., Kodros, J. K., Luo, G., Murphy, D. M., Nault, B. A., Ray, E. A., Weinzierl, B., Wilson, J. C., Yu, F., Yu, P., Pierce, J. R., and Brock, C. A.: A large source of cloud condensation nuclei from new particle formation in the tropics, Nature, 574, 399–403, https://doi.org/10.1038/s41586-019-1638-9, 2019.

https://doi.org/10.5194/egusphere-2025-4338
Preprint. Discussion started: 14 January 2026

Yu, F., Luo, G., Bates, T. S., Anderson, B., Clarke, A., Kapustin, V., Yantosca, R. M., Wang, Y., and Wu, S.: Spatial distributions of particle number concentrations in the global troposphere: Simulations, observations, and implications for nucleation mechanisms, Journal of Geophysical Research: Atmospheres, 115, https://doi.org/https://doi.org/10.1029/2009JD013473, 2010.

Zhang, K., Wan, H., Wang, B., Zhang, M., Feichter, J., and Liu, X.: Tropospheric aerosol size distributions simulated by three online global aerosol models using the M7 microphysics module, Atmospheric Chemistry and Physics, 10, 6409–6434, https://doi.org/10.5194/acp-10-6409-2010, 2010.

Zhao, B., Shrivastava, M., Donahue, N. M., Gordon, H., Schervish, M., Shilling, J. E., Zaveri, R. A., Wang, J., Andreae, M. O., Zhao, C., Gaudet, B., Liu, Y., Fan, J., and Fast, J. D.: High concentration of ultrafine particles in the Amazon free troposphere produced by organic new particle formation, Proceedings of the National Academy of Sciences, 117, 25 344–25 351, https://doi.org/10.1073/pnas.2006716117, 2020.

Zhu, J., Penner, J. E., Yu, F., Sillman, S., Andreae, M. O., and Coe, H.: Decrease in radiative forcing by organic aerosol nucleation, climate, and land use change, Nature Communications, 10, 423, https://doi.org/10.1038/s41467-019-08407-7, 2019.